Alcohol-sourced acetate reduces T cell filamentous actin branching and migration

Vugar Azizov[1,2], Michael Frech[1,2], Jörg Hofmann[3], Marketa Kubankova[4], Dennis Lapuente[5], Matthias Tenbusch[5], Jochen Guck[4], Georg Schett[1,2], and Mario M. Zaiss[1,2] *

[1]Department of Internal Medicine 3, Rheumatology and Immunology, Friedrich-Alexander-University Erlangen-Nürnberg and Universitätsklinikum Erlangen; Erlangen, Germany

[2]Deutsches Zentrum Immuntherapie (DZI), Friedrich-Alexander-University Erlangen-Nürnberg and Universitätsklinikum Erlangen; Erlangen, Germany

[3]Division of Biochemistry, Department of Biology, Friedrich-Alexander-University Erlangen-Nürnberg; Erlangen, Germany

[4]Max Planck Institute for the Science of Light & Max Planck Zentrum für Physik und Medizin; Erlangen, Germany

[5]Institute of Clinical and Molecular Virology, Friedrich-Alexander-University Erlangen-Nürnberg and Universitätsklinikum Erlangen; Erlangen, Germany

*Corresponding author: Mario M. Zaiss

Email: mario.zaiss@uk-erlangen.de

Abstract

Alcohol is among the most widely consumed dietary substances. While excessive alcohol consumption damages the liver, heart and brain, clinical observations also suggest that alcohol has strong immunoregulatory properties. However, little is known about the mechanistic effects of alcohol on the immune system. T cell functions such as migration, immune synapse formation and activation depend on the reorganization of the cytoskeleton. Herein, we show that acetate, the metabolite of alcohol, effectively inhibits the migratory capacity of T cells through increased tissue acetate levels that lead to acetylation of cortactin, a protein that binds filamentous actin and facilitates branching. While acetylation of cortactin reduced actin filament branching, lamellipodia formation and T cell migration, mutated acetylation-resistant cortactin rescued the acetate-induced inhibition of T cell migration. Furthermore, acetate-induced cytoskeletal changes effectively inhibited activation, proliferation, and immune synapse formation in T cells exposed to acetate at tissue concentrations reached by alcohol consumption. In summary, these data show that acetate, the key metabolite of alcohol, is inhibiting T cell mediated immune responses by modulating the biomechanics of T cells through their cytoskeletal function.

Keywords: Alcohol, acetate, cell trafficking, cytoskeleton, filamentous actin, cellular biomechanics

Introduction

For appropriate immune response to occur, immune cells such as T cells, must migrate within and outside of lymphoid organs (Andrian and Mempel, 2003; Burkhardt, 2013; Dupré et al., 2015; Woodland and Kohlmeier, 2009). The cytoskeleton plays a vital role during T cell migration, scanning for antigens, and cell activation (Fowell and Kim, 2021; Mackay et al., 2000; Mastrogiovanni et al., 2020). To migrate, the cytoskeletal structures must remain highly dynamic (Dupré et al., 2015). Failure in cytoskeletal machinery leads to immunodeficiencies due to defects in immune synapse formations, chemotaxis, and migration (Wickramarachchi et al., 2009). Modulation of the components of cytoskeleton via post-translational modifications such as acetylation provides further fine tuning to fit cell's demands (A et al., 2020). Histone deacetylases (HDAC) reverse acetylation of variety of proteins and have been shown to impact immunomodulatory effects of T cells (Akimova et al., 2012). HDAC6 primarily deacetylates cytoskeletal proteins that has been shown to be required for proper immune synapse formation and migration (Luxton and Gundersen, 2007; Regna et al., 2016; Ren et al., 2019; Santo et al., 2012; Serrador et al., 2004; Vishwakarma et al., 2013). For example, pharmacological inhibition of HDAC6 in a preclinical model of systemic lupus erythematosus (SLE) reduced infiltrating T follicular helper (T_{FH}) cells into germinal centers (GC) with significant consequences on autoantibody titers (Regna et al., 2016; Ren et al., 2019). Similarly, we had previously shown that increased exposure to alcohol and alcohol's main metabolite, acetate, affect T_{FH} cell responses in the collagen induced arthritis (CIA) – a mouse model of inflammatory arthritis (Azizov et al., 2020). Mice exposed to either alcohol-sourced or directly supplemented acetate exhibited reduced T_{FH} cell infiltration of B cell follicles and destabilized T_{FH}-B cell conjugate formation both *in vivo* and *in vitro* (Azizov et al., 2020). Consequently, we observed acetate's suppression to be specific to T cell dependent humoral responses both in autoimmune and vaccination mouse models (Azizov et al., 2020). Inhibition of HDAC6 in the context of inflammatory arthritis has been shown to reduce disease severity to levels comparable to dexamethasone treatment (Vishwakarma et al., 2013). Here we hypothesized that the acetate's inhibitory effect could be due to increased acetylation of the cytoskeletal proteins ultimately affecting T cell migration and function. Our hypothesis could explain alcohol's double-edged sword effect in regard to benefits in autoimmunity and damages to health in general (Azizov and Zaiss, 2021; Schuckit, 2009). Alcohol consumption has correlated with decreased severity in rheumatoid arthritis, type 1 diabetes, SLE, and multiple sclerosis in humans as well as in disease mouse models (Azizov and Zaiss, 2021). Upon consumption, alcohol is rapidly metabolized to acetate contributing to increased serum concentrations (Zakhari, 2006). Acetate permeates cells where it is converted to acetyl-Co-enzyme A (acetyl-CoA) and used as a donor for protein acetylation (Bose et al., 2019; Liu et al., 2018). Indeed, increased levels of intracellular acetyl-CoA were linked with significantly higher protein acetylation (Pietrocola et al., 2015). In 2019, Mews and colleagues showed that alcohol consumption can quickly lead to histone acetylation in the brain (Mews et al., 2019). Considering acetate's potential to increase acetylation of intracellular proteins, we set out to investigate whether there is a link between acetate exposure and mitigation of cytoskeletal dynamics in T cells.

Results

Upon alcohol consumption acetate accumulates in lymphoid organs. Building upon our published results, we ventured to study whether the decreased infiltration of GCs by T and B cells along with reduced Tfh-B cell contacts was due to cytoskeletal deficiencies following alcohol-sourced acetate exposure (Azizov et al., 2020). First, we set to quantify the exposure of T cells to acetate upon alcohol consumption by measuring acetate levels in alcohol-impacted and immune relevant lymphoid tissues such as the liver, inguinal lymph node (iLN), and spleen of alcohol-fed mice. We found that acetate indeed accumulates in these organs, especially in lymphoid organs reaching concentrations surpassing 5 mM (Figures 1A-C). Next, we quantified whether or not exposure to 5 mM acetate concentration results in incorporation to cellular metabolism. Previously

it was shown that increased *in vivo* ethanol concentration can lead to an increase in intracellular acetate and citrate (Mews et al., 2019). In an *in vitro* treatment of mouse naïve $CD4^+$ $CD25^-$ $CD44^{low}$ $CD62L^{high}$ T cells, hereafter naïve $CD4^+$ T cells, with ^{13}C labelled acetate, we were able to confirm an increase in ^{13}C containing citrate (Figure 1D). In a subsequent quantification of histone 3 (H3) acetylation levels in the same $CD4^+$ T cells, we observed increased H3 acetylated at lysine 27 (Figure 1E). Together, these findings confirm increased exposure of T cells to acetate, leading to increased protein acetylation within cells.

Exposure to acetate reduces T cell migration capacity. We next performed a trans-well migration assay of either mouse $CD4^+$ or human Jurkat T cells in the presence and absence of acetate. Here we found a significant decrease in trans-well migration of mouse and human derived $CD4^+$ T cells (Figure 1F, 1G). To study the potential impact of decreased T cell migration *in vivo*, primary mouse $CD4^+$ T cells were pre-treated for 4 hours with 5 mM acetate *in vitro*, loaded with CellTrace® dye and combined at 1:1 ratio of control to acetate treated $CD4^+$ T cells, to a total of 6×10^7 cells. We, then, adoptively transferred 6×10^7 cells to recipient C57BL/6 wildtype naïve mice not supplemented with alcohol. 2 hours post adoptive transfer, we observed about 50% decrease in migration of acetate treated $CD4^+$ T cells to spleens of recipient mice compared to control $CD4^+$ T cells (Figure 1H). The same observation was true at 48 hours post adoptive transfer (Figure 1I). These data indicate that the exposure to acetate reduces T cell migration capacity *in vitro* and *in vivo*.

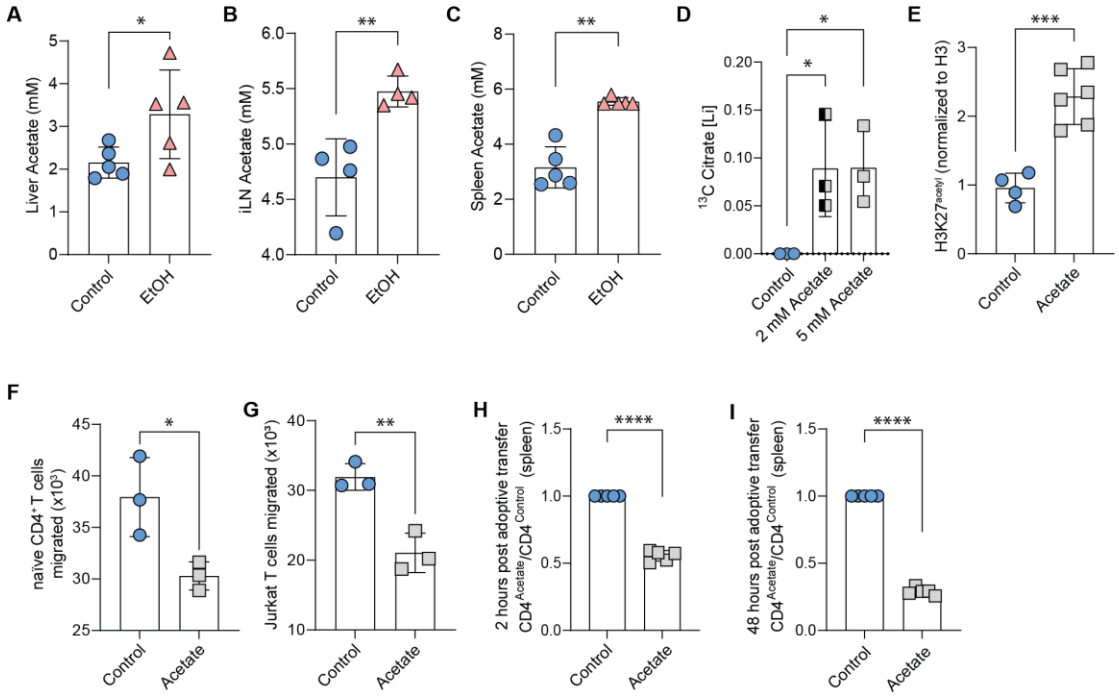

Figure 1. Acetate accumulates in lymphoid organs and impairs T cells migration capacity. GC/MS quantification of acetate in (**A**) livers, (**B**) inguinal lymph nodes (iLN), and (**C**) spleens of alcohol-fed mice compared with water-fed control mice, expressed in mM concentration (individual data point represents one mouse). (**D**) Mouse $CD4^+$ T cells treated *in vitro* with 5 mM ^{13}C labelled acetate exhibit increased ^{13}C labelled citrate, quantified by GC-MS. (**E**) Quantification of western blot analysis of the level of acetylated histone 3 at lysine 27 of mouse $CD4^+$ T cells treated *in vitro* with 5 mM acetate. (**F**) Numbers of migrated mouse naïve $CD4^+$ T cells and (**G**) Jurkat T cells *in vitro* trans-well assay, counted by flow cytometer. (**H**) The ratio of acetate to control treated mouse $CD4^+$ T cells found in the spleens of recipient mice in an adoptive

transfer experiment at 2 hours and (**I**) 48 hours post transfer (each point represents one mouse, n = 5). Data shown from one of two independent experiments (A-C, E, H-I) and combined three independent experiments (D), one of three independent experiments (F, G), and expressed as mean ± SD. Statistical difference was determined by Student's two-tailed t-test. *p < 0.05; **p < 0.01; ***p < 0.001; ****p<0.0001.

T cells exposed to acetate exhibit reduced total filamentous actin. T cells require a dynamic cytoskeleton, especially rapid modifications of filamentous actin (F-Actin), for migration, immune synapse formation and activation (Dupré et al., 2015). Upon quantification of total F-Actin levels by Alexa-Fluor-488™-conjugated phalloidin staining and flow cytometry analysis in mouse naïve $CD4^+$ T cells exposed to 5 mM acetate, we found a dose dependent decrease of F-Actin median fluorescence intensity (MFI) (Figure 2A). F-Actin deficiency also manifests itself by increased cell deformability measured by real-time deformability cytometry (RT-DC) (Golfier et al., 2017). We performed RT-DC and found an increase in T cell deformability upon acetate exposure (Figure 2B). Plotting T cell deformability against cell size sustained the decrease in deformability upon acetate exposure (Figures 2C, 2D). Together these data reveal a reduction of total F-Actin in acetate-exposed T cells.

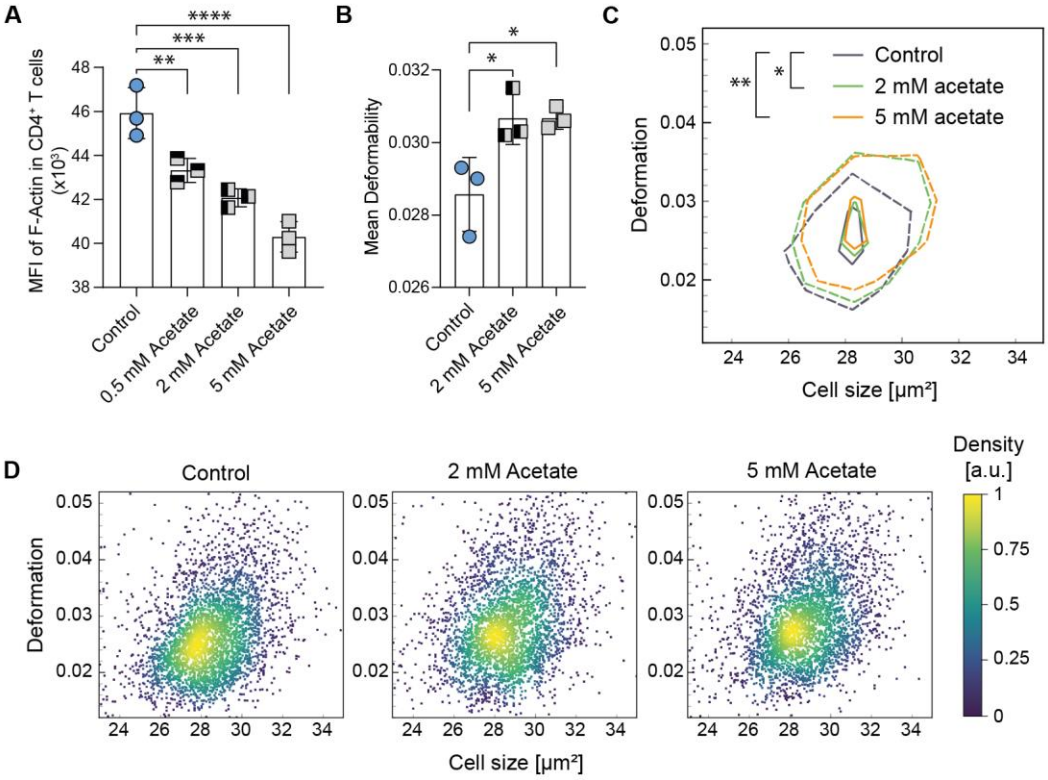

Figure 2. Acetate exposure reduces F-Actin and affects T cell deformability. (**A**) Flow cytometry analysis of mouse $CD4^+$ T cells shows a dose-dependent decrease in phalloidin-Alexa Fluor™-488 median fluorescence intensity (MFI). (**B**) A real-time deformability cytometry (RT-DC) of mouse $CD4^+$ T cells shows an increase in deformability upon 2 mM acetate and 5 mM acetate treatment (n = 3, $CD4^+$ T cells isolated from separate mice). (**C**) Overlay of control, 2 mM and 5 mM acetate treated $CD4^+$ T cell deformation and cell size. (**D**) Scatter plots of RT-DC analysis of control and acetate treated (2 mM and 5 mM) naïve $CD4^+$ T cell deformation shown in Fig. 2C. Data shown from one of three independent experiments (A) and one of two independent experiments (B, C, D) and expressed as mean ± SD. Statistical difference was determined by one-way ANOVA (A, B). Statistical analyses of panel C were carried out using a one-dimensional linear mixed model that incorporates fixed effect parameters and random effects to analyze differences between cell subsets and replicate variances, respectively. *p*-values were determined by a

likelihood ratio test, comparing the full model with a model lacking the fixed effect term. *$p < 0.05$; **$p < 0.01$; ***$p < 0.001$; ****$p<0.0001$.

Exposure to acetate increases acetylation of cortactin in T cells. A recent review article by Mu et al. summarized the acetylation of various components of the cytoskeleton (Mietke et al., 2015). We identified cortactin, a facilitator and stabilizer of F-Actin branching, as a likely candidate for further research as it has acetylation site in each of its 6.5 repeat regions within the actin-filament binding domain (ABD) (A et al., 2020). Most notably, cortactin is also a direct target of HDAC6 (A et al., 2020; Zhang et al., 2007). As pointed out before, treatment of C57BL/6 mice with HDAC6 inhibitor reduced disease severity in a SLE preclinical model and akin to our findings with acetate-exposed collagen induced arthritis (CIA) and T cell dependent vaccination mouse models (Azizov et al., 2020; Regna et al., 2016; Ren et al., 2019). Cortactin acetylation leads to decreased binding to F-Actin and subsequent F-Actin branching (Zhang et al., 2007). Acetate treatment of Jurkat T cells increased acetylation levels of cortactin (Figure 3A). Because acetylation of cortactin prevents its binding to F-Actin, we mutated lysine residues to arginine residues at the acetylation sites (CTTN_KR) within cortactin ABD (Zhang et al., 2007). Microscopy analysis of F-Actin MFI in Jurkat T cells overexpressing CTTN_KR exhibited increased F-Actin amounts even in the presence of acetate (Figure 3B). Further analysis of F-Actin-bound cortactin by Förster Resonance Energy Transfer (FRET) revealed reduced F-Actin-bound cortactin levels upon acetate treatment, and that Jurkat T cells expressing mutated cortactin (CTTN_KR) were resistant to such reduction (Figure 3C). Further, we also quantified acetate's effect on cortactin-F-Actin binding in HEK293T cells and found a similar result (Figure 3D). Next, in trans-well migration assays we found that the expression of acetylation resistant cortactin (CTTN_KR) rescued acetate induced migration deficiency (Figure 3E). Modifications to F-Actin are required for lamellipodia formation and proper T cell migration (Dupré et al., 2015). Cortactin has been shown to be required for lamellipodial persistence and cell migration (Bryce et al., 2005). For this reason, we performed 2D Jurkat T cell tracking in cell culture treated wells by live-cell microscopy (Figure 3F). We found that acetate treated Jurkat T cells had a reduced linearity of forward progression and directional change rate, and that cells expressing acetylation resistant cortactin (CTTN_KR) were resistant to the effects of acetate (Figures 3G, 3H). In order to study the highly dynamic lamellipodia formation and persistence, we generated Jurkat T cells expressing LifeAct-mScarlet-i_N1, a short peptide that binds F-Actin. Here too, we observed reduced lamellipodia formation upon acetate treatment of Jurkat T cells (Figure 3I, 3J and Movie S1). Finally, Western Blot analysis of the splenocytes isolated from alcohol-fed mice exhibited increased levels of acetylated cortactin in comparison to water-fed control mice (Figure 3K). These findings indicate that alcohol consumption can directly increase acetylation of cortactin in secondary lymphoid organs such as spleen and such an increase in T cells impairs T cell migration capacity.

Acetate-induced F-Actin deficiency impairs T cell activation and proliferation. F-Actin cytoskeleton is required for T cell – antigen presenting cell (APC) interaction and immune synapse formation (Colin-York et al., 2019; Fritzsche et al., 2017; Valitutti et al., 1995). Therefore, we performed co-culturing experiment of NP-CGG antigen-pulsed dendritic cells (DCs) and $CD4^+$ T cells in order to interrogate if acetate-directed F-Actin deficiency affects T cell activation. T cells were either pre-treated with 5 mM acetate or vehicle, while antigen-pulse of DCs with NP-CGG was performed in an absence of acetate. Later upon combining DCs and T cells, acetate treatment was continued in an effort to replicate *in vivo* acetate exposure within lymphoid organs. Here, flow cytometry analysis revealed reduced surface CD69 levels on acetate treated $CD4^+$ $CD25^+$ T cells indicating reduced activation (Figure 4A). In the same experiment, flow cytometry analysis of acetate treated $CD4^+$ T cells revealed that Ki67 levels, a proliferation marker, were reduced (Figure 4B). Next, we performed confocal fluorescence microscopy to visualize F-Actin at the immune synapse by phalloidin staining and quantified MFI values. There was a decrease in F-Actin accumulation at the immune synapses within T cells between T cells and DCs (Figure 4C). Activation of naïve $CD4^+$ T cells with anti-CD3 and anti-CD28 antibody coated beads in the presence of acetate also resulted in reduced F-Actin amounts, as quantified by Alexa-Fluor-488™-

phalloidin MFI (Figure 4D). These experiments document the sensitivity of T cells to cytoskeletal deficiencies for migration, immune synapse formation, and activation, and they shed light on our previously published finding of reduced Tfh-B cell conjugate formation upon acetate exposure *in vivo* and *in vitro* (Azizov et al., 2020).

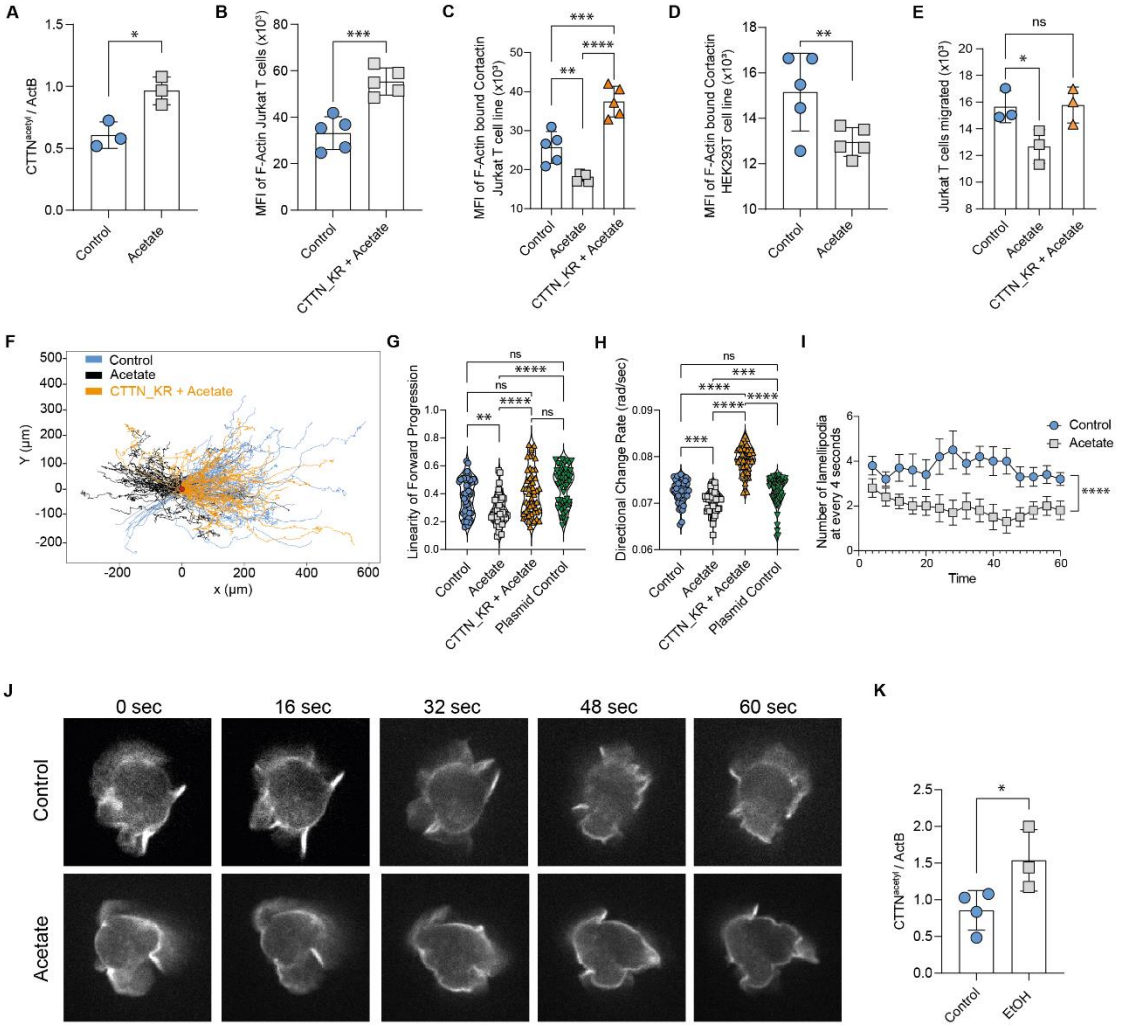

Figure 3. Acetylation resistant cortactin rescues acetate-induced migration deficiency. (**A**) Quantification of western blot analysis of the level of acetylated cortactin in Jurkat T cells treated with 5 mM acetate. (**B**) MFI of F-Actin in acetate treated Jurkat T cells overexpressing CTTN_KR in comparison to control Jurkat T cells. (**C**) MFI of Förster Resonance Energy Transfer (FRET) from F-Actin bound cortactin in Jurkat T cells quantified by confocal scanning laser microscopy in control and acetate treatment, as well as in acetate treated Jurkat T cells expressing acetylation resistant cortactin (CTTN_KR). (**D**) MFI of Förster Resonance Energy Transfer (FRET) from F-Actin bound cortactin in control and acetate treated HEK293T cells quantified by confocal laser scanning microscopy. (**E**) Numbers of migrated Jurkat T cells *in vitro* trans-well assay of control, acetate treated, as well as acetate treated Jurkat T cells expressing acetylation resistant cortactin (CTTN_KR). (**F**) Individual tracks analyzed in panel G and H. (**G**) Linearity of forward progression and (**H**) directional change rate of Jurkat T cells treated with 5 mM acetate, medium control, plasmid electroporation control and Jurkat T cells expressing CTTN_KR and individual cells tracked by Image J Fiji TrackMate plugin [28, 29] (n = 50 cells). (**I**) Numbers of lamellipodia per 4-second time points in LifeAct-mScarlet expressing Jurkat T cells upon control and acetate treatment (n = 10 cells). (**J**) Representative still images of control and acetate treated LifeAct-mScarlet expressing Jurkat T cells at 0, 16, 32, 48, and 60th seconds (for

full movie see Movie S1). (**K**) Quantification of western blot analysis of the level of acetylated cortactin in the splenocytes of alcohol-fed mice compared to water-fed control (n = 4 control mice, n = 3 alcohol-fed mice (EtOH)). Data shown from one of three independent experiments (C, E) and one of two independent experiments (A, B, D, F, G, H, K, I, J) and expressed as mean±SD, except for panels G and H where data are expressed as mean±SEM. Statistical difference was determined by Student's two-tailed t-test (A, B, D, K), one-way ANOVA (C, E, G, H) and area under the curve analysis (I). *$p < 0.05$; **$p < 0.01$; ***$p < 0.001$; ****$p<0.0001$.

Acetate-exposed mice exhibit inhibited T cell responses in the lungs upon influenza infection. In an effort to study the effect of alcohol-sourced acetate on T cell migration during viral infection, we utilized mouse influenza infection model. Here, alcohol consuming mice were infected with influenza H1N1 and two weeks later lungs isolated. Flow cytometry analysis revealed reduced numbers of $CD8^+$ $CD69^+$ $CD103^+$ T cells in the lungs of alcohol consuming influenza infected mice in comparison to water-fed control mice (Figure 4E). Interestingly, we also found decreased percentage of $CD69^+$ Tet^+ influenza specific $CD8^+$ T cells and $CD69^+$ $CD8^+$ T cells in alcohol consuming influenza infected mice in contrast to water-fed control mice (Figures 4F, 4G). In addition, we observed reduced percentage of $CXCR3^+$ $CD8^+$ T cells in the lungs of alcohol consuming mice in comparison with water-fed control mice (Figure 4H). Flow cytometry analysis of the $CD4^+$ T cells in the lungs, revealed a reduction in percentage of $CD69^+$ and also $CXCR3^+$ $CD4^+$ T cells in alcohol consuming mice in contrast to water-fed control mice (Figures 4I, 4J). Together these data reflect deficiencies in T cell migration, activation, and function.

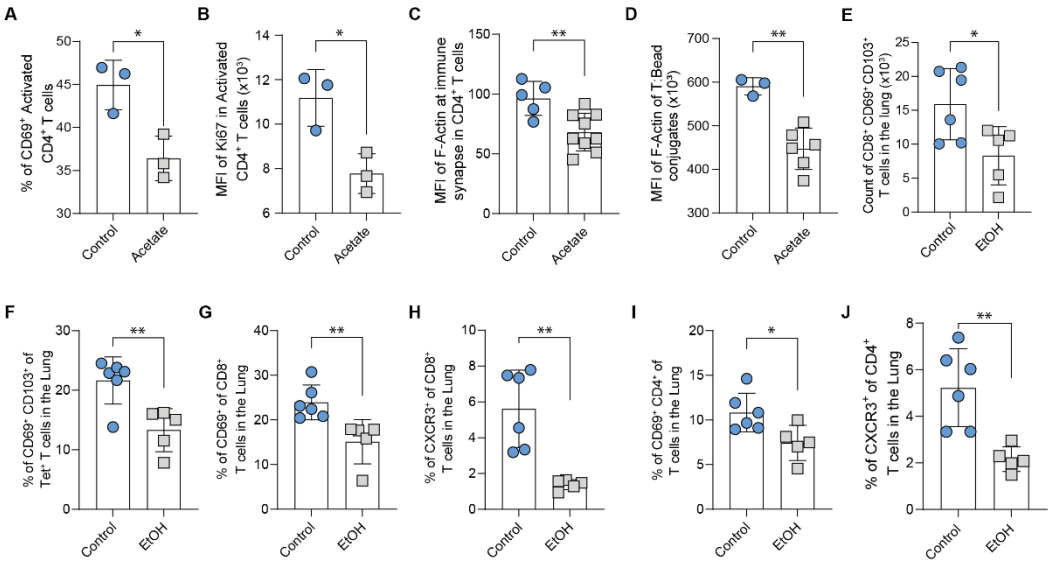

Figure 4. Acetate-induced F-Actin deficiency reduces T cell activation and proliferation.
(**A**) Flow cytometry analysis of percentage of $CD69^+$ $CD25^+$ $CD4^+$ and (**B**) Ki67 MFI of $CD4^+$ T cells *in vitro* co-culture with NP-CGG pulsed DCs in the presence or absence of 5 mM acetate. (**C**) MFI of F-Actin accumulated in $CD4^+$ T cells at the immune synapse with NP-CGG pulsed DCs quantified by confocal laser scanning microscopy and (**D**) with mouse $CD4^+$ T cell activator beads quantified by flow cytometry. Flow cytometry analysis of $CD69^+$ $CD103^+$ (**E**) $CD8^+$ T cells and (**F**) influenza specific tetramer (Tet^+) $CD8^+$ T cells in the lungs of alcohol-fed mice in comparison to water-fed control mice. (**G**) Flow cytometry analysis of percentage of $CD69^+$ and (**H**) percentage of $CXCR3^+$ of $CD8^+$ T cells in the lungs of alcohol-fed mice in comparison to water-fed control mice. (**I**) Flow cytometry analysis of percentage of $CD69^+$ and (**J**) percentage of $CXCR3^+$ of $CD4^+$ T cells in the lungs of alcohol-fed mice in comparison to water-fed control mice (each point represents one mouse. n = 6 control, n = 5 alcohol-fed mice). Data shown from one of three independent experiments (A, B, D), two independent experiments (C, E, F, G, H, I, J) and expressed as mean ± SD. Statistical difference was determined by Student's two-tailed t-test. *$p < 0.05$; **$p < 0.01$; ***$p < 0.001$; ****$p < 0.0001$.

Discussion

Our findings indicate that alcohol-sourced acetate accumulates in lymphoid organs, increases cellular acetylated-cortactin levels preventing F-Actin branching and impeding T cell migration (overview Fig. 5). The Arp2/3 complex is a part of F-Actin branching nucleator complex (Fritzsche et al., 2017). But it does require cortactin to facilitate its binding to F-Actin. Whereas cortactin was shown to increase the affinity of Arp2/3 complex for F-Actin by almost 20-fold (Uruno et al., 2001). In addition, cortactin plays a key role in linking cortical F-Actin to the cell membrane (Weed and Parsons, 2001). Inhibition of Arp2/3 complex formation reduced T cell deceleration upon encountering high affinity antigens to a level observed for low affinity antigens (Moreau et al., 2015). This finding potentially explains the weak immune synapse formation in our current study and also reduced T_{FH}-B cell conjugate formation upon acetate exposure in our previously published findings (Azizov et al., 2020). F-Actin rearrangement enables cells to migrate, direct adhesion molecules to cell-cell contact zones, divide, and regulate various other cellular processes (Roy and Burkhardt, 2018; Stricker et al., 2010). Cytoskeleton is one of the central elements for optimum T cell function (Huang and Burkhardt, 2007). For example, functional actin cytoskeleton has been shown to be important for T cell sampling of antigen-MHCII complexes on APCs with subsequent role in immune synapse formation (Valitutti et al., 1995). $CD4^+$ and $CD8^+$ T cell migration patterns through secondary lymphoid organs (SLOs) differ, $CD4^+$ T cells spend more time probing MHCII molecules presented on DCs and are significantly faster in entering and exiting SLOs than $CD8^+$ T cells (Fricke et al., 2016; Gérard et al., 2014; Mandl et al., 2012). It is possible that diminished F-Actin branching can therefore mitigate TCR coupling with high-affinity antigens and reduce T cell arrest and subsequent activation. Interestingly, in a mouse model of type 1 diabetes, mice fed with acetate-yielding chow exhibited a reduction in autoreactive T cells (both $CD4^+$ and $CD8^+$) and ultimately reduced the incidence of the disease (Mariño et al., 2017). In another study of experimental autoimmune encephalomyelitis (EAE), cortactin knock-out mice exhibited decreased incidence, disease severity, and infiltration of the central nervous system by $CD4^+$ T cells (Samus et al., 2020). Interestingly, we observed the same effect in alcohol-fed EAE mice (Azizov et al., 2020). In an influenza infection model, alcohol-fed mice exhibited decreased homing to lungs, reduced CD69, CD103, and CXCR3 positive tissue resident $CD8^+$ T cells. Cortactin is overexpressed in B cells of chronic lymphoblastic leukemia patients (CLL), implicated in T cell acute lymphoblastic leukemia (T-ALL), and promotes migration in cancer (Schnoor et al., 2018; Zhang et al., 2009). Identification of an Achille's heal of T cell migration, motility, and immune synapse formation can set the stage for pharmacological and/or natural targeting in cases of autoimmunity. Further, such interventions can also help improve immune responses to vaccinations. In an evolutionary perspective, hominids adapted to alcohol metabolism by feeding on fermenting fruits from the forest floor (Carrigan et al., 2015). It is possible that indirect alcohol consumption mitigated adverse immune responses in early humans under high microbial load. Today, we see the same effects reflected in mitigation of autoimmunity and susceptibility to infections amongst alcohol consumers (Szabo, 1999).

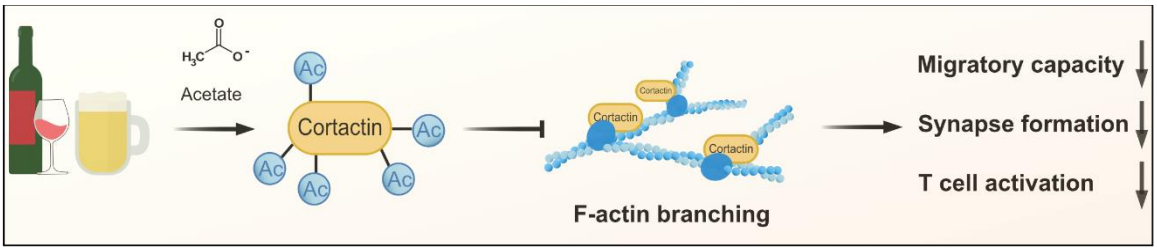

Figure 5. Overview of the mode of acetate's action on T cell F-Actin reorganization.
Alcohol consumption results in accumulation of acetate in lymphoid organs, increases acetylated cortactin levels in T cells. This results in reduced F-Actin branching and consequently reduced migratory capacity, synapse formation, and activation.

Movie S1. Jurkat T cells exposed to acetate exhibit reduced lamellipodia formation.
Jurkat T cells expressing LifeAct-mScarlet treated with 5 mM acetate or vehicle (R10 medium) in R10 medium (n = 10 cells per treatment), visualized at 6 frames per second (each frame = 4 seconds) for 60 seconds. Stills included as Fig. 3J.

Materials and Methods

Mice. Female, 6 weeks old C57BL/6NCrl mice were purchased from Charles River (Germany). Mice were co-housed for 3 weeks prior to start of experiments. All mice were housed, and experiments were conducted under specific pathogen-free conditions. All of the protocols for animal experiments were approved by the local ethics authorities of the Regierung von Unterfranken (55.2-2532-2-703, 55.2.2-2532-2-1515).

Adoptive transfer experiments. $CD4^+$ T cells (naïve or total) were enriched with naïve or total $CD4^+$ T cell negative enrichment kits (Stemcell, Biolegend) from the spleens of female, 8 weeks old C57BL/6NCrl mice. T cells were then either treated with 5 mM sodium acetate or sodium matched R10 medium (RPMI 1640, 10% v/v Fetal Bovine Serum, supplemented with 50 µM β-mercaptoethanol, non-essential amino acids, 2 mM L-Glutamine, sodium pyruvate, 10 mM HEPES, and 1% penicillin and streptomycin) for 4 hours. Cells were spun down (300xg) and washed two times with PBS at room temperature (RT). Cells were then loaded with CellTrace® cell dye (CFSE and Violet, for control and acetate treatment) according to manufacturer's instructions (Thermo Fisher) and incubated further 30 minutes with corresponding treatment (control or acetate containing R10 medium). Cells were then counted and adjusted to 3x107 cells for each treatment and combined to make $6x10^7$ cells in PBS prior to transfer to recipient mice (C57BL/6NCrl, female, matching age) intravenously in the tail-vain. Recipient mice were sacrificed 2 hours and 48 hours post adoptive transfer, and spleens collected for flow cytometry.

NP-CGG Immunizations. Female, 8 weeks old C57BL/6NCrl mice were co-housed and 1 week before immunization, mice were given either water, 10% (v/v) Ethanol (Roche) and 2% (w/v) Glucose (Sigma), all feedings were changed every 3 days. For primary NP-CGG immunization, mice were injected intraperitoneally (i.p.) with 100 µg of NP-CGG (LGC Biosearch Technologies) in 200 µL of alum (Thermo Scientific) according to manufacturer's instructions. 14 days later, mice were boosted with 100 µg of NP-CGG in 200 µL of alum. One week later, mice were sacrificed, and spleens collected for isolation of $CD4^+$ T cells and dendritic cells (Stemcell, Biolegend) for *in vitro* experiments.

Influenza infection model. Starting 1 week before infection, C57BL/6NCrl mice were given either 2% (w/v) Glucose water or 10% (v/v) Ethanol (Roche) and 2% (w/v) Glucose (Sigma). All feedings were changed every 3 days and were continued throughout the infection. Animals were infected by intranasal instillation of 200 PFU of H1N1 A/Puerto Rico/8/1934 in 50 µL PBS under general anesthesia. Lungs were harvested 14 days post infection. For T cell analyses, lungs were cut in pieces and were treated with 500 units Collagenase D and 160 units DNase I in 2 mL R10 medium (RPMI 1640 supplemented with 10% FCS, 2 mM L-Glutamine, 10 mM HEPES, 50 µM β-mercaptoethanol and 1% penicillin/streptomycin) for 45 minutes at 37°C. Lungs were then mashed through a 70 µm cell strainer before subjected to erythrocyte lysis. One fifth of the cell suspension was stained with a pentamer for NP366-374-specific $CD8^+$ T cells (1:40; ProImmune), anti-CD8-BV711 (1:300, clone 53-6.7, Biolegend), anti-CD4-BV605 (1:300, clone RM4-5, Biolegend), anti-CD45-BV510 (1:300, clone 30F11, Biolegend), anti-CD69-PerCP-Cy5.5 (1:200, clone H12F3, Biolegend), anti-CD103-PE (1:200, clone 2E7, Invitrogen), anti-CXCR3-APC-Fire750 (1:100, clone CXCR3-173, Biolegend), anti-CD127-FITC (1:300, clone A7R34, Biolegend), and anti-KLRG1-PE-Cy7 (1:300, clone 2F1, Invitrogen). Data were acquired on an AttuneNxt (ThermoFisher) and analysed using FlowJo™ software (Tree Star Inc.).

Flow cytometry. Spleens were smashed and filtered through 40 µm gauze (BD Biosciences). Single-cell suspensions were incubated with antibodies for 30 minutes at 4°C, washed and analyzed with Cytoflex S flow cytometer (Beckman Coulter). Flow cytometry analysis of *in vitro* experiments were performed by centrifuging cells in 96-well V-bottom plates at 300xg and 4°C for 5 minutes. Antibody staining for surface markers were performed at 4°C for 30 minutes, followed by two times wash with FACS Buffer (PBS, 2 mM EDTA, 2% Fetal Bovine Serum) and one-time

wash with PBS. Cells were then resuspended in 100 µL of PBS and fixed with addition of 100 µL of IC Fixation Buffer (Thermo Fisher) and incubated at 4°C for 15 minutes protected from light. Cells were then washed three times with 1x Permeabilization buffer and incubated for 1 hour at RT for permeabilization (Thermo Fisher) followed by intracellular staining. Intracellular staining of filamentous actin was performed by incubating cells with phalloidin-Alexa-Fluor®-488 (Abcam) at 1:1000 dilution for 2 hours at RT in PBS with 1% w/v BSA, protected from light.

***In vitro* migration.** Jurkat T cells or naïve $CD4^+$ T cells were treated with 5 mM sodium acetate containing R10 medium for 4 hours prior to Transwell migration assay. T cells were then seeded at 105 cells in 100 µL total volume above 3 µm and 8 µm pore size transwell inserts (GreinerBio), mouse $CD4^+$ T cells and Jurkat T cells, respectively. Transwell inserts were placed in 24-well plate containing R10 medium matching the volume height within the insert (600 µL) and incubated for 4 hours. Migrated cells were collected from the bottom wells and centrifuged, resuspended in 100 µl FACS buffer, quantified by flow cytometry.

***In vitro* co-culture of Antigen Presenting Cells (APCs) and T cells.** Dendritic cells (DCs) and $CD4^+$ T cells were enriched from C57BL/6CNrl mice immunized two times, 14 days apart, with 100 µg NP-CGG in 200 µL of Imject™ Alum and sacrificed on day 21 (Stemcell, Thermo Fisher, LGC). $CD4^+$ T cells were pre-treated with 0.5, 2.0, or 5 mM sodium acetate or vehicle (R10 medium) containing R10 medium for 4 hours. Meanwhile, DCs were pulsed with 20 µg/mL NP-CGG (LGC) and 100 ng/mL LPS (Sigma Aldrich) in R10 medium for 4 hours. $CD4^+$ T cells were adjusted to 105 cells per well of 96-well flat bottom cell culture plate. DCs were then washed two times with fresh medium and combined with $CD4^+$ T cells for 48 hours. Final total volume per well was 200 µL. At the conclusion of 48-hour incubation, cells were moved to a 96-well V-bottom cell culture plate, wells flushed and collected. Cells were fixed and stained as explained under Flow Cytometry section.

***In vitro* activation of $CD4^+$ T cells.** Naïve $CD4^+$ T cells were enriched from C57BL/6CNrl mice (Stemcell). Then, the cells were pre-treated with 0.5, 2.0, or 5 mM sodium acetate or vehicle (R10 medium) containing R10 medium for 4 hours. Dynabeads™ Mouse T-Activator CD3/CD28 beads were added according to manufacturer's instructions for 4 hours (Thermo Fisher). At the conclusion of 4 hours, cells were centrifuged at 4°C at 200xg for 10 minutes and fixed with IC fixation buffer (Thermo Fisher) in 200 µL (100 µL IC Fixation buffer + 100 µL PBS) for 15 minutes at 4°C. Following fixation, cells were washed with PBS three times and permeabilized with 1x eBiosciences™ permeabilization buffer for 1 hour at room temperature (Thermo Fisher). Phalloidin-iFluor 488 (Abcam) stock solution was diluted in PBS containing 1% w/v BSA 1000x. After permeabilization, cells were washed three times and Phalloidin-iFluor 488 solution added for 2 hours at RT.

Immune synapse formation. Dendritic cells (DCs) and $CD4^+$ T cells were enriched from C57BL/6CNrl mice immunized two times, 14 days apart, with 100 µg NP-CGG in 200 µL of Imject™ Alum and sacrificed on day 21 (Stemcell, Thermo Fisher, LGC). $CD4^+$ T cells were pre-treated with 0.5, 2.0, 5.0 mM acetate or vehicle (R10 medium) for 6 hours in R10 medium. Simultaneously, DCs were pulsed with 20 µg/mL NP-CGG in R10 medium for 6 hours. Then, 10^6 pre-treated naïve $CD4^+$ T cells and 10^6 NP-CGG pulsed DCs were combined in 100 µL of R10 medium for 15 minutes at 37°C. Then 1.5 mL of 1.5% paraformaldehyde (PFA) was added to arrest T-DC conjugates. Cells were then washed with PBS+2% FCS (v/v) three times. Cells were then stained for flow cytometry with anti-mouse CD4 BV421™ and anti-mouse CD11c BV510™, or for microscopy anti-CD4 Alexa Fluor 647™ only in PBS+2% FCS (v/v) for 30 minutes at 4°C. Cells were washed, and fixed with eBiosciences™ IC fixation buffer for 15 minutes at 4°C. Cells were washed with PBS three times and permeabilized with 1x eBiosciences™ permeabilization buffer for 1 hour at room temperature. Phalloidin-iFluor 488 stock solution was diluted in PBS containing 1% w/v BSA 1000x. After permeabilization, cells were washed three times and Phalloidin-iFluor 488 solution added for 2 hours at RT. Then, cells were washed with PBS three

times with 5-minute incubations in PBS to remove all unbound Phalloidin-iFluor 488. For microscopy samples, nuclei were staining with DAPI in PBS for 5 minutes and then washed and resuspended in 60 µL of PBS. Drops of 30 µL were placed on microscope slides and allowed to dry in the dark. After, ProLong™ Glass Anti-fade mounting medium was used to mount slides and let cure for 24 hours. Samples for flow cytometry were resuspended after washing Phalloidin-iFluor 488 out and resuspending in PBS.

Live cell tracking. Jurkat T cells and Jurkat T cells overexpressing acetylation resistant cortactin (CTTN_KR) were cultured in R10 medium supplemented with 5 mM sodium acetate for 4 hours. For acetate treatment control, Jurkat T cells were cultured in R10 medium. As a control for plasmid electroporation, Jurkat T cells electroporated with mScarlet_H plasmid were used. The cells were then transferred to incubated and CO2 gassed Zeiss Cell Discoverer (Carl Zeiss) live imaging microscope. Then images were taken by brightfield illumination with Apochromat 10x objective in 2-minute intervals for a total of 180 minutes. Cells were then tracked using TrackMate plugin for Fiji (Schindelin et al., 2012; Tinevez et al., 2017). To visualize individual tracks, tracks were obtained from TrackMate and re-centered at the origin of the plot.

Live cell imaging of lamellipodia. Jurkat T cells overexpressing pLifeAct_mScarlet-i_N1 (see Electroporation methods), were treated with 5 mM sodium acetate or vehicle (R10 medium) containing R10 medium for 4 hours. Later, cells were seeded into µ-Slide 8 well microscope slides (ibidi) and placed into incubated microscopy chamber. Zeiss Spinning Disc Axio observer Z1 microscope with oil immersed 63x 1.2 NA objective and EVOLVE 512 EMCCD with Yokogawa CSU-X1M 5000 was used to locate cells. Cells were illuminated with a laser at 561 nm wavelength, and emissions captured through band-pass filter 629/62 every 4 seconds for 60 seconds. Images were later processed and analyzed for numbers of lamellipodia at each time point and counted. Statistical analysis was done by area under the curve analysis.

Cortactin lysine to arginine mutagenesis. Recombinant cortactin gene with lysine residues 87, 124, 161, 198, 235, 272, 309, and 319 replaced with arginine, was synthesized, and cloned into pcDNA3.1plus vector by GeneArt™ Thermo Fisher. Jurkat T cells were electroporated as described below and clones were selected with 800 µg/mL G418 (InvivoGen) antibiotic for 7 passages.

Electroporation of Jurkat T cells. Jurkat T cells were maintained in R10 medium. 107 Jurkat T cells were washed two times with RPMI1640 medium only, centrifugation steps at 200xg for 10 minutes, at RT. Jurkat T cells were then washed one more time with 5 mL of OptiMEM® medium and resuspended in 100 µL of OptiMEM® medium. 25 µg (1 µg/µL concentration) of plasmid DNA was added to electroporation 4 mm cuvettes (Bio-Rad) first and then cells added to the cuvettes. Electroporation was carried out with Bio-Rad Gene Pulser Xcell Electroporation Systems at Square wave, 500 Volts, 3 ms, Pulse 1, Interval 0). After the electroporation, cells were transferred to T25 cell culture flasks with 5 mL of prewarmed (37°C) R10 medium and incubated overnight. For control purposes, no plasmid DNA containing cell mixture was used for electroporation.

Real-time Deformability Cytometry (RT-DC). RT-DC measurements were performed using an AcCellerator instrument (Zellmechanik Dresden). T cells were resuspended in measurement buffer composed of 0.6% (m/v) methyl cellulose dissolved in phosphate-buffered saline adjusted to a viscosity of 60 mPa s at 24°C using a falling ball viscometer (Haake; Thermo Fisher Scientific). The suspension of T cells was loaded into a 1 mL syringe attached to a syringe pump and connected by PEEK-tubing (IDEX Health & Science) to a microfluidic chip made of PDMS bonded on cover glass. A second syringe with pure measurement buffer was attached to the chip. The microfluidic chip consisted of two inlets and one outlet. The measurement was performed in a narrow channel constriction of 15 × 15 µm square cross section. The total flow rate was 0.024 µL/s, with sheath flow rate of 0.018 µL/s and sample flow rate of 0.006 µL/s. Measurement

temperature was 28°C. Images were acquired at a frame rate of 1250 fps. Cells were detected in a region of interest of 250 × 80 pixels. The cell images were analyzed using the analysis software Shape-Out version 2.3.0 (available at https://github.com/ZELLMECHANIK-DRESDEN/ShapeOut2) and Python 3.7 using dclab library. We applied a gate for cross-sectional cell size (15-35 μm^2) and for the area ratio (1–1.05). The calculation of deformation, a measure of how much the cell shape deviates from circularity, was obtained from the image using the projected area and cell contour length calculated from the convex hull. Statistical analyses were carried out using a one-dimensional linear mixed model that incorporates fixed effect parameters and random effects to analyze differences between cell subsets and replicate variances, respectively. p-values were determined by a likelihood ratio test, comparing the full model with a model lacking the fixed effect term.

Protein Isolation and Western Blot. After acetate treatment of Jurkat T cells, naïve CD4+ T cells activated either with 0.5 µg/mL PMA, 1 µg/mL ionomycin or NP-CGG-pulsed CD11c+ DCs then depleted off DCs, T cells were washed two times with ice-cold PBS containing 5 mM sodium butyrate, and nuclear/cytoplasmic protein was extracted according to manufacturer's instructions (Thermo Fisher). Protein fractions were then frozen and stored at -80°C until analyzed by western blotting. Protein extracts were separated on 4-12% Bis-Tris gradient SDS-polyacrylamide gel, then transferred onto PVDF membrane, blocked with 5% milk in TBS 0.05% Tween 20 for 1 hour. Then membranes were probed with anti-cortactin, anti-acetyl cortactin, anti-GAPDH, anti-beta-actin, anti-histone 3, anti-acetyl-lysine-27-histone-3, and anti-histone 3 antibodies, and visualized with appropriate HRP-conjugated secondary antibody. The signal acquired from chemiluminescence (Celvin S) for protein of interests were optimized to loading control and quantified with Image J blot analysis tool.

Histone extraction. Naïve $CD4^+$ T cells were pre-treated with 0.5, 2.0, 5.0 mM sodium acetate or vehicle (R10 medium) containing R10 medium for 4 hours. Cells were then washed with ice cold PBS supplemented with 5 mM sodium butyrate to preserve histone acetylation. Then the cytoplasm was extracted by resuspending cells in ice cold extraction buffer at 107 cell/mL, incubating on ice for 5 minutes, and centrifuging at 6500xg for 10 minutes at 4°C. Supernatant was discarded and the cytoplasm extracted for the second time. Histones were extracted by resuspending the pellet in 0.25 M HCl at a density of $4x10^7$ cells/mL. Samples were then sonicated for 30 seconds, placed on ice, then sonicated for further 30 seconds. Afterwards, tubes were placed on rollers at 4°C for 1 hour. Then, samples were centrifuged at 12000xg for 10 minutes at 4°C. Supernatant was collected and neutralized with 2M NaOH at 1/10th of the volume of the supernatant. Extracted histones were frozen and stored at -80°C until analyzed by western blotting.

Protein isolation from splenocytes. Spleens of alcohol-fed and water-fed C57BL/6NCrl mice were isolated and placed in ice cold PBS containing 5 mM sodium butyrate after 3 weeks of feeding at steady-state. Spleens were smashed and filtered through 40 µm gauze (BD Biosciences). Single-cell suspensions were spun down and resuspended in 5 mL of 1x Red Blood Cell Lysis buffer (Biolegend) and incubated on ice for 5 minutes with occasional swirl. Then, 25 mL of ice-cold PBS was added, and cells centrifuged at 300xg for 10 minutes. Cells were resuspended in 10 mL ice-cold PBS and spun down. Protein isolation of cytoplasmic and nuclear fraction was performed with NE-PER™ Nuclear Cytoplasmic Extraction (Thermo Fisher) supplemented with Pierce™ Protease inhibitor cocktail tablet (Thermo Fisher). Isolated proteins were kept at -80°C until analyzed by western blotting.

^{13}C Citrate quantification. Label incorporation into citrate was analyzed by gas chromatography (GC – MS). In brief, cells were subjected to methanol-chloroform-water extraction and polar phase was dried under vacuum. For derivatization, 20 µL per sample of 40 mg methoxamine per mL pyridine were added and incubated at 30°C for 90 minutes, followed by the addition of 80 µL per sample of MSTFA, incubated at 37°C for 60 minutes. GC-MS analysis was performed on an

Agilent 7890B GC – Pegasus 4D-C GCxGC TOF MS, coupled to a Gerstel autosampler. Samples were injected in splitless mode (injection volume 1 µL). The following temperature program was applied during sample injection: initial temperature of 80°C for 3 seconds followed by a ramp of 7°C/seconds to 210°C and final hold for 3 minutes. Gas chromatographic separation was performed with a Rxi-5MS column (30 m length, 250 µm inner diameter, 0.25 µm film thickness (Restek). Helium was used as carrier gas with a flow rate of 1.2 mL/minute. Gas chromatographic separation was performed with the following temperature gradient: 2 minutes initial hold at 68°C, first temperature gradient with 5°C/minute up to 120°C, second temperature gradient with 7°C/minute up to 200°C, and a third temperature gradient with 12°C/minute up to 320°C with a final hold for 6 minutes. The spectra were recorded in a mass range of 60 to 600 m/z with an acquisition rate of 20 spectra/second. Data was analyzed with ChromaTOF (Leco) and MetMax software (Kempa et al., 2009).

Short-Chain Fatty Acid (SCFA) measurements. 4-5 biological replicates of each treatment (control or ethanol feeding) mouse spleens were placed directly into diethyl ether and weighed in a 2 mL polypropylene tube. The tubes were kept in a cool rack throughout the extraction. 50 µL 33% HCl was added, and samples were vortexed for 1 minute and centrifuged for 3 minutes at 4°C. The organic phase was transferred into a 2 mL gas chromatography (GC) vial. For the calibration curve, 100 µl of SCFA calibration standards (Sigma) were dissolved in water to concentrations of 0, 0.5, 1, 5 and 10 mM and then subjected to the same extraction procedure as the samples. For GCMS analysis 1 µl of the sample (4-5 replicates) was injected with a split ratio of 20:1 on a Famewax, 30 m x 0,25 mm iD, 0.25 µm df capillary column (Restek). The GC-MS system consisted of GCMS QP2010Plus gas chromatograph/ mass spectrometer coupled with an AOC20S autosampler and an AOC20i auto injector (Shimadzu). Injection temperature was 240°C with the interface set at 230°C and the ion source at 200°C. Helium was used as carrier gas with constant flow rate of 1 mL/min. The column temperature program started with 40°C and was ramped to 150°C at a rate of 7 °C/min and then to 230°C at a rate of 9 °C/min, and finally held at 230°C for 9 minutes. The total run time was 40 minutes. SCFA were identified based on the retention time of standard compounds and with the assistance of the NIST 08 mass spectral library. Full scan mass spectra were recorded in the 25-150 m/z range (0.5 s/scan). Quantification was done by integration of the extracted ion chromatogram peaks for the following ion species: m/z 45 for acetate eluted at 7.8 minutes, m/z 74 for propionate eluted at 9.6 minutes, and m/z 60 for butyrate eluted at 11.5 minutes. GCMS solution software was used for data processing.

Plasmids. pLifeAct_mScarlet-i_N1 (Addgene plasmid # 85056 ; http://n2t.net/addgene:85056; RRID:Addgene_85056) and pmScarlet-H_C1 (Addgene plasmid # 85043; http://n2t.net/addgene:85043 ; RRID:Addgene_85043) was a gift from Dorus Gadella (Bindels et al., 2017). CTTN_KR plasmid was synthesized and cloned into pcDNA3.1plus vector by GeneArt™ Thermo Fisher.

Statistical analysis. Data are expressed as mean±SD unless otherwise indicated in the figure legend. Analysis was performed using a two-sided Student's t test, single comparison or analysis of variance test for multiple comparisons (one-way or two-way ANOVA followed by Tukey's or Bonferroni's multiple comparisons test, respectively). All experiments were conducted at least two times, unless otherwise indicated in the figure legends. n-numbers denote number of individual animals or cells isolated from individual animals. P-values of 0.05 were considered significant and are shown as $p < 0.05$ (*), $p < 0.01$ (**), $p < 0.001$ (***), $p < 0.0001$ (****). Graph generation and statistical analyses were performed using Prism version 8 software (GraphPad).

Data availability. The data that support the findings of this study are available from the corresponding author upon reasonable request by email to mario.zaiss@uk-erlangen.de.

Acknowledgments

We thank Schimpf M., Danzer H. and Steffen F. for technical assistance. We also thank Schmidt K. and Harrer T. for their help with T cell electroporation. We are grateful to Dürholz K., Schälter F., Saad M.S.A., Vogg M., Ramming A., Weidner D. for their support and help with experiments. We thank Geisberger S. and Kempa S. for ^{13}C Citrate quantification and data analysis. We thank Tripal P. Winter Z. and Schmidt B. from the OICE in Erlangen for technical expertise. We thank Mielenz D., Sarter K., and Brandl C., for helpful discussions.

Author Contributions: Conceptualization: VA, GS, MMZ. Methodology: VA, MF, JH, MK, DL. Investigation: VA, MK, MT, MMZ. Visualization: VA, MF, MK. Funding acquisition: GS, MMZ. Project administration: VA, MMZ. Supervision: MMZ. Writing – original draft: VA, MMZ. Writing – review & editing: VA, MT, JG, GS, MMZ

Competing Interest Statement: Authors declare that they have no competing interests.

References

A, M., Latario, C.J., Pickrell, L.E., and Higgs, H.N. (2020). Lysine acetylation of cytoskeletal proteins: Emergence of an actin code. J Cell Biol *219*, e202006151. https://doi.org/10.1083/jcb.202006151.

Akimova, T., Beier, U.H., Liu, Y., Wang, L., and Hancock, W.W. (2012). Histone/protein deacetylases and T-cell immune responses. Blood *119*, 2443–2451. https://doi.org/10.1182/blood-2011-10-292003.

Andrian, U.H. von, and Mempel, T.R. (2003). Homing and cellular traffic in lymph nodes. Nat Rev Immunol *3*, 867–878. https://doi.org/10.1038/nri1222.

Azizov, V., and Zaiss, M.M. (2021). Alcohol Consumption in Rheumatoid Arthritis: A Path through the Immune System. Nutrients *13*, 1324. https://doi.org/10.3390/nu13041324.

Azizov, V., Dietel, K., Steffen, F., Dürholz, K., Meidenbauer, J., Lucas, S., Frech, M., Omata, Y., Tajik, N., Knipfer, L., et al. (2020). Ethanol consumption inhibits TFH cell responses and the development of autoimmune arthritis. Nat Commun *11*, 1998. https://doi.org/10.1038/s41467-020-15855-z.

Bindels, D.S., Haarbosch, L., Weeren, L. van, Postma, M., Wiese, K.E., Mastop, M., Aumonier, S., Gotthard, G., Royant, A., Hink, M.A., et al. (2017). mScarlet: a bright monomeric red fluorescent protein for cellular imaging. Nat Methods *14*, 53–56. https://doi.org/10.1038/nmeth.4074.

Bose, S., Ramesh, V., and Locasale, J.W. (2019). Acetate Metabolism in Physiology, Cancer, and Beyond. Trends Cell Biol *29*, 695–703. https://doi.org/10.1016/j.tcb.2019.05.005.

Bryce, N.S., Clark, E.S., Leysath, J.L., Currie, J.D., Webb, D.J., and Weaver, A.M. (2005). Cortactin Promotes Cell Motility by Enhancing Lamellipodial Persistence. Curr Biol *15*, 1276–1285. https://doi.org/10.1016/j.cub.2005.06.043.

Burkhardt, J.K. (2013). Cytoskeletal function in the immune system. Immunol Rev *256*, 5–9. https://doi.org/10.1111/imr.12121.

Carrigan, M.A., Uryasev, O., Frye, C.B., Eckman, B.L., Myers, C.R., Hurley, T.D., and Benner, S.A. (2015). Hominids adapted to metabolize ethanol long before human-directed fermentation. Proc National Acad Sci *112*, 458–463. https://doi.org/10.1073/pnas.1404167111.

Colin-York, H., Javanmardi, Y., Skamrahl, M., Kumari, S., Chang, V.T., Khuon, S., Taylor, A., Chew, T.-L., Betzig, E., Moeendarbary, E., et al. (2019). Cytoskeletal Control of Antigen-Dependent T Cell Activation. Cell Reports *26*, 3369-3379.e5. https://doi.org/10.1016/j.celrep.2019.02.074.

Dupré, L., Houmadi, R., Tang, C., and Rey-Barroso, J. (2015). T Lymphocyte Migration: An Action Movie Starring the Actin and Associated Actors. Front Immunol *6*, 586. https://doi.org/10.3389/fimmu.2015.00586.

Fowell, D.J., and Kim, M. (2021). The spatio-temporal control of effector T cell migration. Nat Rev Immunol *21*, 582–596. https://doi.org/10.1038/s41577-021-00507-0.

Fricke, G.M., Letendre, K.A., Moses, M.E., and Cannon, J.L. (2016). Persistence and Adaptation in Immunity: T Cells Balance the Extent and Thoroughness of Search. Plos Comput Biol *12*, e1004818. https://doi.org/10.1371/journal.pcbi.1004818.

Fritzsche, M., Fernandes, R.A., Chang, V.T., Colin-York, H., Clausen, M.P., Felce, J.H., Galiani, S., Erlenkämper, C., Santos, A.M., Heddleston, J.M., et al. (2017). Cytoskeletal actin dynamics shape a ramifying actin network underpinning immunological synapse formation. Sci Adv *3*, e1603032. https://doi.org/10.1126/sciadv.1603032.

Gérard, A., Patino-Lopez, G., Beemiller, P., Nambiar, R., Ben-Aissa, K., Liu, Y., Totah, F.J., Tyska, M.J., Shaw, S., and Krummel, M.F. (2014). Detection of Rare Antigen-Presenting Cells through T Cell-Intrinsic Meandering Motility, Mediated by Myo1g. Cell *158*, 492–505. https://doi.org/10.1016/j.cell.2014.05.044.

Golfier, S., Rosendahl, P., Mietke, A., Herbig, M., Guck, J., and Otto, O. (2017). High-throughput cell mechanical phenotyping for label-free titration assays of cytoskeletal modifications. Cytoskeleton *74*, 283–296. https://doi.org/10.1002/cm.21369.

Huang, Y., and Burkhardt, J.K. (2007). T-cell-receptor-dependent actin regulatory mechanisms. J Cell Sci *120*, 723–730. https://doi.org/10.1242/jcs.000786.

Kempa, S., Hummel, J., Schwemmer, T., Pietzke, M., Strehmel, N., Wienkoop, S., Kopka, J., and Weckwerth, W. (2009). An automated GCxGC-TOF-MS protocol for batch-wise extraction and alignment of mass isotopomer matrixes from differential 13C-labelling experiments: a case study for photoautotrophic-mixotrophic grown Chlamydomonas reinhardtii cells. J Basic Microb *49*, 82–91. https://doi.org/10.1002/jobm.200800337.

Liu, X., Cooper, D.E., Cluntun, A.A., Warmoes, M.O., Zhao, S., Reid, M.A., Liu, J., Lund, P.J., Lopes, M., Garcia, B.A., et al. (2018). Acetate Production from Glucose and Coupling to Mitochondrial Metabolism in Mammals. Cell *175*, 502-513.e13. https://doi.org/10.1016/j.cell.2018.08.040.

Luxton, G.W.G., and Gundersen, G.G. (2007). HDAC6-Pack: Cortactin Acetylation Joins the Brew. Dev Cell *13*, 161–162. https://doi.org/10.1016/j.devcel.2007.07.014.

Mackay, I.R., Rosen, F.S., Andrian, U.H. von, and Mackay, C.R. (2000). T-Cell Function and Migration — Two Sides of the Same Coin. New Engl J Medicine *343*, 1020–1034. https://doi.org/10.1056/nejm200010053431407.

Mandl, J.N., Liou, R., Klauschen, F., Vrisekoop, N., Monteiro, J.P., Yates, A.J., Huang, A.Y., and Germain, R.N. (2012). Quantification of lymph node transit times reveals differences in antigen surveillance strategies of naïve CD4+ and CD8+ T cells. Proc National Acad Sci *109*, 18036–18041. https://doi.org/10.1073/pnas.1211717109.

Mariño, E., Richards, J.L., McLeod, K.H., Stanley, D., Yap, Y.A., Knight, J., McKenzie, C., Kranich, J., Oliveira, A.C., Rossello, F.J., et al. (2017). Gut microbial metabolites limit the frequency of autoimmune T cells and protect against type 1 diabetes. Nat Immunol *18*, 552–562. https://doi.org/10.1038/ni.3713.

Mastrogiovanni, M., Juzans, M., Alcover, A., and Bartolo, V.D. (2020). Coordinating Cytoskeleton and Molecular Traffic in T Cell Migration, Activation, and Effector Functions. Frontiers Cell Dev Biology *8*, 591348. https://doi.org/10.3389/fcell.2020.591348.

Mews, P., Egervari, G., Nativio, R., Sidoli, S., Donahue, G., Lombroso, S.I., Alexander, D.C., Riesche, S.L., Heller, E.A., Nestler, E.J., et al. (2019). Alcohol metabolism contributes to brain histone acetylation. Nature *574*, 717–721. https://doi.org/10.1038/s41586-019-1700-7.

Mietke, A., Otto, O., Girardo, S., Rosendahl, P., Taubenberger, A., Golfier, S., Ulbricht, E., Aland, S., Guck, J., and Fischer-Friedrich, E. (2015). Extracting Cell Stiffness from Real-Time Deformability Cytometry: Theory and Experiment. Biophys J *109*, 2023–2036. https://doi.org/10.1016/j.bpj.2015.09.006.

Moreau, H.D., Lemaître, F., Garrod, K.R., Garcia, Z., Lennon-Duménil, A.-M., and Bousso, P. (2015). Signal strength regulates antigen-mediated T-cell deceleration by distinct mechanisms to promote local exploration or arrest. Proc National Acad Sci *112*, 12151–12156. https://doi.org/10.1073/pnas.1506654112.

Pietrocola, F., Galluzzi, L., Bravo-San Pedro, J.M., Madeo, F., and Kroemer, G. (2015). Acetyl Coenzyme A: A Central Metabolite and Second Messenger. Cell Metab *21*, 805–821. https://doi.org/10.1016/j.cmet.2015.05.014.

Regna, N.L., Vieson, M.D., Luo, X.M., Chafin, C.B., Puthiyaveetil, A.G., Hammond, S.E., Caudell, D.L., Jarpe, M.B., and Reilly, C.M. (2016). Specific HDAC6 inhibition by ACY-738 reduces SLE pathogenesis in NZB/W mice. Clin Immunol *162*, 58–73. https://doi.org/10.1016/j.clim.2015.11.007.

Ren, J., Catalina, M.D., Eden, K., Liao, X., Read, K.A., Luo, X., McMillan, R.P., Hulver, M.W., Jarpe, M., Bachali, P., et al. (2019). Selective Histone Deacetylase 6 Inhibition Normalizes B Cell Activation and Germinal Center Formation in a Model of Systemic Lupus Erythematosus. Front Immunol *10*, 2512. https://doi.org/10.3389/fimmu.2019.02512.

Roy, N.H., and Burkhardt, J.K. (2018). The Actin Cytoskeleton: A Mechanical Intermediate for Signal Integration at the Immunological Synapse. Frontiers Cell Dev Biology *6*, 116. https://doi.org/10.3389/fcell.2018.00116.

Samus, M., Li, Y.-T., Sorokin, L., Rottner, K., and Vestweber, D. (2020). Actin-Binding Protein Cortactin Promotes Pathogenesis of Experimental Autoimmune Encephalomyelitis by Supporting

Leukocyte Infiltration into the Central Nervous System. J Neurosci *40*, 1389–1404. https://doi.org/10.1523/jneurosci.1266-19.2019.

Santo, L., Hideshima, T., Kung, A.L., Tseng, J.-C., Tamang, D., Yang, M., Jarpe, M., Duzer, J.H. van, Mazitschek, R., Ogier, W.C., et al. (2012). Preclinical activity, pharmacodynamic, and pharmacokinetic properties of a selective HDAC6 inhibitor, ACY-1215, in combination with bortezomib in multiple myeloma. Blood *119*, 2579–2589. https://doi.org/10.1182/blood-2011-10-387365.

Schindelin, J., Arganda-Carreras, I., Frise, E., Kaynig, V., Longair, M., Pietzsch, T., Preibisch, S., Rueden, C., Saalfeld, S., Schmid, B., et al. (2012). Fiji: an open-source platform for biological-image analysis. Nat Methods *9*, 676–682. https://doi.org/10.1038/nmeth.2019.

Schnoor, M., Stradal, T.E., and Rottner, K. (2018). Cortactin: Cell Functions of A Multifaceted Actin-Binding Protein. Trends Cell Biol *28*, 79–98. https://doi.org/10.1016/j.tcb.2017.10.009.

Schuckit, M.A. (2009). Alcohol-use disorders. Lancet *373*, 492–501. https://doi.org/10.1016/s0140-6736(09)60009-x.

Serrador, J.M., Cabrero, J.R., Sancho, D., Mittelbrunn, M., Urzainqui, A., and Sánchez-Madrid, F. (2004). HDAC6 Deacetylase Activity Links the Tubulin Cytoskeleton with Immune Synapse Organization. Immunity *20*, 417–428. https://doi.org/10.1016/s1074-7613(04)00078-0.

Stricker, J., Falzone, T., and Gardel, M.L. (2010). Mechanics of the F-actin cytoskeleton. J Biomech *43*, 9–14. https://doi.org/10.1016/j.jbiomech.2009.09.003.

Szabo, G. (1999). CONSEQUENCES OF ALCOHOL CONSUMPTION ON HOST DEFENCE. Alcohol Alcoholism *34*, 830–841. https://doi.org/10.1093/alcalc/34.6.830.

Tinevez, J.-Y., Perry, N., Schindelin, J., Hoopes, G.M., Reynolds, G.D., Laplantine, E., Bednarek, S.Y., Shorte, S.L., and Eliceiri, K.W. (2017). TrackMate: An open and extensible platform for single-particle tracking. Methods *115*, 80–90. https://doi.org/10.1016/j.ymeth.2016.09.016.

Uruno, T., Liu, J., Zhang, P., Fan, Y., Egile, C., Li, R., Mueller, S.C., and Zhan, X. (2001). Activation of Arp2/3 complex-mediated actin polymerization by cortactin. Nat Cell Biol *3*, 259–266. https://doi.org/10.1038/35060051.

Valitutti, S., Dessing, M., Aktories, K., Gallati, H., and Lanzavecchia, A. (1995). Sustained signaling leading to T cell activation results from prolonged T cell receptor occupancy. Role of T cell actin cytoskeleton. J Exp Medicine *181*, 577–584. https://doi.org/10.1084/jem.181.2.577.

Vishwakarma, S., Iyer, L.R., Muley, M., Singh, P.K., Shastry, A., Saxena, A., Kulathingal, J., Vijaykanth, G., Raghul, J., Rajesh, N., et al. (2013). Tubastatin, a selective histone deacetylase 6 inhibitor shows anti-inflammatory and anti-rheumatic effects. Int Immunopharmacol *16*, 72–78. https://doi.org/10.1016/j.intimp.2013.03.016.

Weed, S.A., and Parsons, J.T. (2001). Cortactin: coupling membrane dynamics to cortical actin assembly. Oncogene *20*, 6418–6434. https://doi.org/10.1038/sj.onc.1204783.

Wickramarachchi, D.C., Theofilopoulos, A.N., and Kono, D.H. (2009). Immune pathology associated with altered actin cytoskeleton regulation. Autoimmunity *43*, 64–75. https://doi.org/10.3109/08916930903374634.

Woodland, D.L., and Kohlmeier, J.E. (2009). Migration, maintenance and recall of memory T cells in peripheral tissues. Nat Rev Immunol *9*, 153–161. https://doi.org/10.1038/nri2496.

Zakhari, S. (2006). Overview: How Is Alcohol Metabolized by the Body? Alcohol Research and Health *29*, 245–254. .

Zhang, X., Yuan, Z., Zhang, Y., Yong, S., Salas-Burgos, A., Koomen, J., Olashaw, N., Parsons, J.T., Yang, X.-J., Dent, S.R., et al. (2007). HDAC6 Modulates Cell Motility by Altering the Acetylation Level of Cortactin. Mol Cell *27*, 197–213. https://doi.org/10.1016/j.molcel.2007.05.033.

Zhang, Y., Zhang, M., Dong, H., Yong, S., Li, X., Olashaw, N., Kruk, P.A., Cheng, J.Q., Bai, W., Chen, J., et al. (2009). Deacetylation of cortactin by SIRT1 promotes cell migration. Oncogene *28*, 445–460. https://doi.org/10.1038/onc.2008.388.